

Dual-mode on-demand droplet routing in multiple microchannels using a magnetic fluid as carrier phase

Jitae Kim,¹ June Won,² and Simon Song^{1,2,a)}

¹*Institute of Nano Science and Technology, Hanyang University, Seoul 133-791, South Korea*

²*Department of Mechanical Convergence Engineering, Hanyang University, Seoul 133-791, South Korea*

(Received 10 July 2014; accepted 22 August 2014; published online 8 September 2014)

We present dual-mode, on-demand droplet routing in a multiple-outlet microfluidic device using an oil-based magnetic fluid. Magnetite (Fe_3O_4) nanoparticle-contained oleic acid (MNOA) was used as a carrier phase for droplet generation and manipulation. The water-in-MNOA droplets were selectively distributed in a curved microchannel with three branches by utilizing both a hydrodynamic laminar flow pattern and an external magnetic field. Without the applied magnetic field, the droplets travelled along a hydrodynamic centerline that was displaced at each bifurcating junction. However, in the presence of a permanent magnet, they were repelled from the centerline and diverted into the desired channel when the repelled distance exceeded the minimum offset allocated to the channel. The repelled distance, which is proportional to the magnetic field gradient, was manipulated by controlling the magnet's distance from the device. To evaluate routing performance, three different sizes of droplets with diameters of 63, 88, and 102 μm were directed into designated outlets with the magnet positioned at varying distances. The result demonstrated that the 102- μm droplets were sorted with an accuracy of $\sim 93\%$. Our technique enables on-demand droplet routing in multiple outlet channels by simply manipulating magnet positions (active mode) as well as size-based droplet separation with a fixed magnet position (passive mode). © 2014 AIP Publishing LLC. [<http://dx.doi.org/10.1063/1.4894748>]

INTRODUCTION

Droplet-based microfluidics has recently drawn considerable attention due to its unique approach to processing chemical/biological assays^{1–3} and synthesizing functional micro/nanoparticles.^{4,5} A large number of monodisperse droplets, ranging from nano- to picoliters in volume, can be generated using flow-focusing or T-junction geometry, and each of these droplets can serve as an individual reaction vessel. Such a microfluidic droplet approach allows for reduced consumption of sample and reagents as well as reduced analysis time. These advantages make droplet microfluidics highly useful, particularly for high throughput applications, such as cell screening assay⁶ and drug discovery.⁷

In an effort to develop droplet manipulation techniques that are useful for conducting complex chemical and biological studies, various operation modules have been demonstrated, including droplet fusion,⁸ fission,⁹ mixing,¹⁰ and sorting.^{11,12} Among these modules, droplet sorting is one of the most important operations, and has been accomplished by utilizing various means, including a membrane valve,¹³ surface acoustic wave,¹⁴ dielectrophoresis,¹⁵ Marangoni effect,¹⁶ and magnetic field.^{17–22}

The microfluidic droplet sorting methods can be classified into two categories: passive and active. One popular sorting scheme relies on channel geometry and droplet size. This is a

^{a)} Author to whom correspondence should be addressed. Electronic mail: simonsong@hanyang.ac.kr. Tel.: 82-2-2220-0423. Fax: 82-2-2298-4634.

passive technique that involves a bifurcation where two channels of different widths and/or lengths depart to generate an asymmetric flow division. Tan *et al.*²³ employed a bifurcating junction to sort larger droplets into the narrower outlet channel while smaller ones were moved in the wider outlet channel. The size-based droplet sorting was achieved based on shear stress exerted on droplets and flow rate difference among the outlet channels. Though simple and robust to implement, passive sorting techniques are limited to droplets with a certain size range due to the fixed geometry of the channels. Nevertheless, those techniques were frequently adapted for continuous, self-regulated separation of particles^{24,25} and droplets.²⁶ For example, isolation of droplets containing circulating tumor cells from a whole blood suspension was demonstrated using hydrodynamic effects,²⁷ in which droplets were sorted based on the size of the cells they contained. This method allowed continuous, label-free separation of droplets encapsulating a single cell with an efficiency of 70–80%.

Active sorting techniques generally utilize external forces or energies applied to droplets. For instance, magnetic force has been exploited to manipulate droplets incorporating magnetic nanoparticles, called magnetic droplets. Zhang *et al.*¹⁹ showed a T-junction microfluidic device in which droplets containing magnetite (Fe_3O_4) nanoparticles (MN) were deflected into designated channels using permanent magnets. The magnet's position relative to the device was changed to control the deflection of the droplets, permitting a relatively high throughput at a rate of 10 droplets per second. Although the superparamagnetic nanoparticles exhibited little magnetic hysteresis with high biocompatibility, their application to biological assays in this format could be limited due to high costs and interference imposed by the use of high particle loadings of up to 40 mg ml^{-1} . The same research group also reported various microfluidic droplet operation units²⁰ using oil-based ferrofluid. Since the ferrofluid was used as continuous phase, water droplets were repelled from the magnet's surface and the repulsion of the droplets was controlled by translating the magnet. The magnetic repulsion-based droplet manipulation had an apparent advantage over most active sorting methods because the content of a droplet is unaffected by external stimuli, such as temperature and electric current that could disturb biological assays. It should be noted that the magnetic repulsion of droplets falls in the narrow distance range of $\sim 250 \mu\text{m}$ for a given magnet, which may restrict its use to a device with up to a few outlets or a device requiring coarse control only. Hence it is expected to improve the utility of the repulsion-based droplet sorter if an additional scheme like passive hydrodynamic effect is added. This will require minimal repelling distances when sorting droplets in a microfluidic device with multiple outlets or with a wide channel. Moreover, a droplet sorter that can be alternately operated in passive and active control modes will be beneficial for complex chemical/biological applications.

In this paper, we present dual-mode, on-demand droplet routing in a curved microchannel with four outlets (one main and three side channels) using a magnetic fluid of oleic acid (OA) containing MN, called "MNOA." The main focus of this work is to investigate the behavior of water-in-MNOA droplets under both hydrodynamic flow conditions (passive mode) and an external magnetic field (active mode), and also to demonstrate droplet routing in a multiple-outlet device by exploiting these two effects. To this end, both simulation and visual assessment were performed on the hydrodynamic flow that governed the droplet's path in the absence of magnetic fields. Then, lateral deflections of the droplets were examined with a disc magnet positioned at varying distances from the channel. Routing conditions for each side channel were established through characterization of the droplet behaviors in both the presence and absence of the magnet. Then, routing performance was tested for three different sizes of droplets and evaluated based on the routing conditions. This routing module will be useful for separation of multiple targets from a multi-component sample or stratification of droplets in response to multiple stimuli from a single-component sample.

PRINCIPLE

Routing at a single bifurcation

The principle of on-demand droplet routing is depicted in Fig. 1. Routing is achieved by utilizing both a hydrodynamic laminar flow pattern and magnet-based droplet repulsion. In a

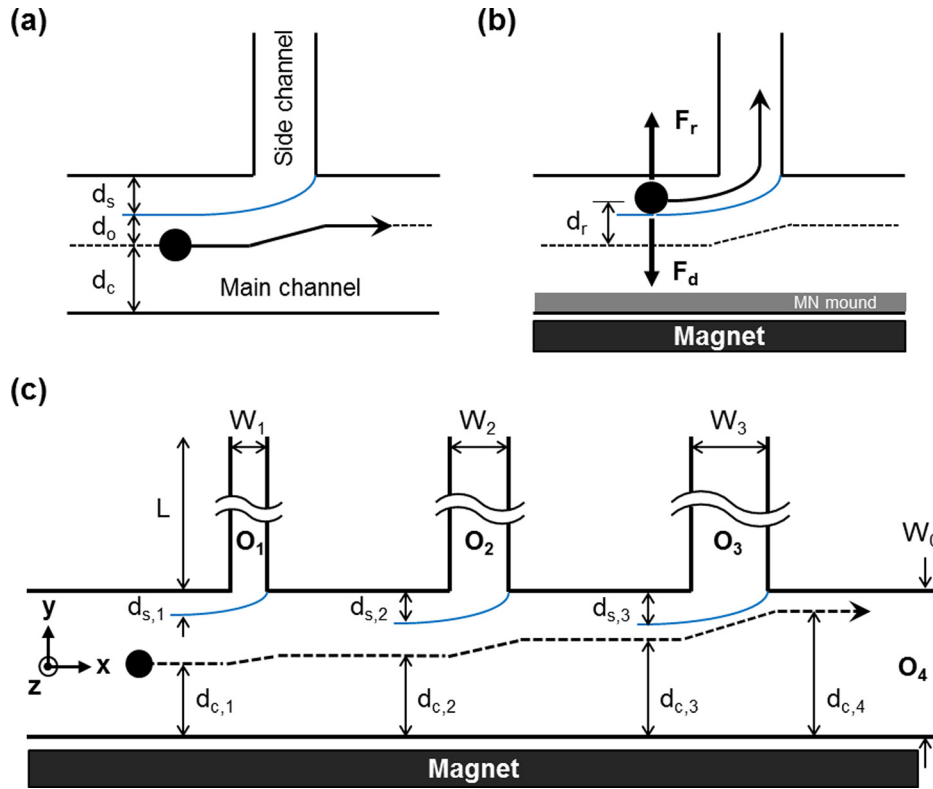


FIG. 1. Schematic diagrams illustrating the droplet behaviors at bifurcating junction geometries (top view). The main channel is wider than the side channel. Fluids enter the main channel from the left side and exit the side and main channels. The filled circle is a water-in-MNOA droplet. The blue line is a virtual boundary that distinguishes between side channel and main channel flow. (a) In the absence of a magnet, the droplet moves along the hydrodynamic centerline which is displaced upward at the junction. (b) In the presence of a magnet, the droplet is repelled away from the magnet while MN mound is formed at the lower wall. The droplet is diverted into the side channel when repelling force is sufficiently strong (i.e., $d_r > d_o$). F_r denotes the droplet repelling force and F_d denotes the Stokes drag. The magnetic field lines point into and out of the plane of the drawing. (c) Droplet behavior in a main channel with three side channels (four outlets, O_1 through O_4). The side channels have the same length (L) and different widths ($W_1 < W_2 < W_3$). The dotted arrow represents the droplet trajectory in the absence of a magnet. The magnet is moved along the z -direction (i.e., out of the plane) with its edges aligned with the bottom wall of the main channel.

microchannel with a side channel, a laminar flow is divided into two flow streams at the junction as shown in Fig. 1(a). The blue line is a virtual boundary that separates a layer of fluid that diverts into the side channel from the main channel. The distance from the blue line to the upper wall (d_s) is determined by the relative flow rate distribution into the side channel. Because of the flow division, the hydrodynamic centerline is displaced in the direction of the side channel at the junction. The distance between the centerline and the lower wall (d_c) also depends on the hydrodynamic parameters of the laminar flow. In the absence of a magnetic field, a water-in-MNOA droplet moves along the hydrodynamic centerline of the main channel without being diverted into the side channel. No diversion will occur until the channel dimensions are arranged such that the virtual boundary and hydrodynamic centerline overlap (i.e., $d_o = 0$).

With its presence, the magnetic susceptibility of the water droplet ($\chi_p \sim -10^{-5}$, dimensionless) is much smaller than that of the ferromagnetic MNOA medium ($\chi_m \sim 0.11$). This means that the droplet is repelled away from the region of highest magnetic field (i.e., a magnet's surface), while MN are attracted to the region, forming a MN mound along the lower wall (see Fig. 1(b)). Accordingly, the repelling force on a water-in-MNOA droplet could be expressed as²⁸

$$F_r = \frac{V \cdot \Delta X}{\mu_0} (B \cdot \nabla) B, \quad (1)$$

where V is the volume of a droplet (m^3), $\Delta\chi$ is the difference in magnetic susceptibility ($\chi_p - \chi_m$), μ_0 is the magnetic permeability of the vacuum ($4\pi \times 10^{-7} \text{ H m}^{-1}$), B is the magnetic flux density (T), and ∇B is the magnetic field gradient (T m^{-1}). As shown in Fig. 1(b), if the repelled distance (d_r) of a droplet from the centerline is greater than the minimum offset distance required for diversion (i.e., $d_r > d_o$), the droplet will be placed inside the virtual boundary and thus diverted into the side channel.

Routing at multiple bifurcations

As an extension of the single bifurcation case, a main (wider) channel with three side (narrower) channels is discussed for routing water-in-MNOA droplets. The side channels are designed to have the same lengths (L), but different widths ($W_1 < W_2 < W_3$). As shown in Fig. 1(c), the hydrodynamic centerline is displaced upward at each bifurcating junction (i.e., $d_{c,1} < d_{c,2} < d_{c,3} < d_{c,4}$) when the flow direction is from the left to right side. Also, the distances of each blue line from the upper wall increase (i.e., $d_{s,1} < d_{s,2} < d_{s,3}$) because the flow rate ratios of the main channel to each consecutive side channel decrease. This configuration leads to a progressive reduction in minimum offset distance corresponding to each side channel (i.e., $d_{o,1} > d_{o,2} > d_{o,3}$ where $d_{o,i} = W_0 - d_{c,i} - d_{s,i}$). Assuming that a droplet moves along the hydrodynamic centerline, the dotted arrow represents the droplet's trajectory in the absence of a permanent magnet. In the case of applying magnetic fields, water-in-MNOA droplets divert into one of the four outlets (O_1 through O_4) based on the following condition:

$$d_{o,i} < d_r < d_{o,i-1} \quad (i = 1, 2, 3, 4), \quad (2)$$

where the diversion occurs at an outlet (O_i) corresponding to the subscript i .

According to the magnetization curve (see Fig. S1 in the supplementary material³⁰), the MN reached magnetic saturation at $\sim 90 \text{ mT}$. If applied magnetic field strengths are above this level, the magnetic repelling force only depends on the gradient of the magnetic flux density ($F_r \sim \nabla B$) for a given size droplet. The gradient (∇B) is in turn related to the inverse of the distance of the magnet's surface from the microchannels (see Fig. S2 in the supplementary material³⁰). This relation suggests that the magnitude of the repelling force and the repelled distance of a droplet can be tuned by varying the relative position of the magnet. Hence routing water-in-MNOA droplets into a designated outlet can be achieved by manipulating repelled distances (d_r) and minimum offsets (d_o). Note that the minimum offsets are designed to have different values for each side channel by the fixed hydrodynamic flow patterns, which are fixed by the channel arrangement, while the repelled distances can be varied by the magnet position according to routing requirements.

Estimation of virtual boundary position (d_s)

In a pressure-driven, laminar flow in the microchannels (w_0 and w_n are the widths of main and n th side channel, and h is the height), a parabolic velocity profile can be assumed as

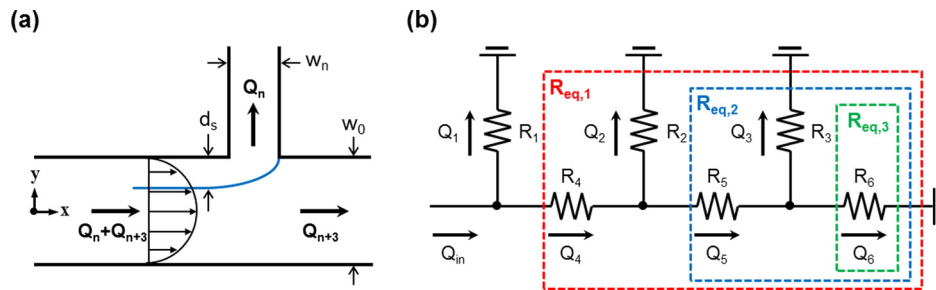


FIG. 2. (a) Schematic (top view) of flow geometry at the n th bifurcation. (b) Electrical circuit analogy to the microchannel network.

illustrated in Fig. 2(a). A virtual boundary position from the upper wall (d_s) is calculated with the flow rate ratio of the main to side channel flows represented by Poiseuille's equation,

$$FR_n \equiv \frac{Q_n}{Q_n + Q_{n+3}} = \frac{\frac{w_0}{2\mu} \int_{d_s}^{\frac{w_0}{2}} \left(-\frac{\partial p}{\partial x} \right) \left(\frac{w_0^2}{4} - y^2 \right) dy}{\frac{w_0}{2\mu} \int_{-\frac{w_0}{2}}^{\frac{w_0}{2}} \left(-\frac{\partial p}{\partial x} \right) \left(\frac{w_0^2}{4} - y^2 \right) dy}, \quad (3)$$

where μ is the fluid viscosity. Using an equivalent electrical circuit model of the microfluidic network shown in Fig. 2(b), the flow rate ratio can be expressed in terms of hydraulic resistances of each channel

$$FR_n = \frac{1/R_n}{1/R_n + 1/R_{eq,n}} \quad (n = 1, 2, \text{ and } 3), \quad (4)$$

$R_{eq,n}$ is the equivalent resistance corresponding to dotted rectangles, and each $R_{eq,n}$ is given as

$$R_{eq,1} = R_4 + \frac{1}{1/R_2 + 1/R_{eq,2}}, \quad (5)$$

$$R_{eq,2} = R_5 + \frac{1}{1/R_3 + 1/R_{eq,3}}, \quad (6)$$

$$R_{eq,3} = R_6. \quad (7)$$

Also, R_n can be obtained by using the hydraulic resistance equation²⁹

$$R_n = \frac{12\mu L}{h^3 w \left[1 - \frac{192}{\pi^5} \sum_{n, \text{odd}}^{\infty} \frac{h}{w} \tan h \left(h\pi \frac{w}{2h} \right) \right]}. \quad (8)$$

Then, the flow rate ratios at each bifurcation are determined as $FR_1 = 0.1046$, $FR_2 = 0.1546$, and $FR_3 = 0.1692$. Using these values, the virtual boundary positions are obtained as $d_{s,1} = 80 \mu\text{m}$, $d_{s,2} = 99 \mu\text{m}$, and $d_{s,3} = 105 \mu\text{m}$.

EXPERIMENTAL

Materials

A magnetite (Fe_3O_4) nanoparticle solution was purchased from Sigma-Aldrich (07318, MO, USA). They were coated with oleic acid, and the solution contained heptane as a stabilizer. The concentration and mean diameter of the nanoparticles were 7.59 mg ml^{-1} and $6.5 \pm 3.0 \text{ nm}$, respectively. Oleic acid ($\rho = 890 \text{ kg m}^{-3}$ and $\eta = 0.033 \text{ Pa s}$) was purchased from Daejung Chemicals & Metals (Seoul, Korea). NdFeB disc magnets (8.5 mm diameter \times 4 mm height) were purchased from Dongnam Co. (Seoul, Korea). Sylgard[®] 184 Silicone Elastomer Kit, obtained from Dow Corning (MI, USA), was used for polydimethylsiloxane (PDMS) microchannel preparation. See the online supplementary material³⁰ for further information on the magnetite nanoparticles and disk magnet's flux density.

Preparation of MNOA

Heptane was present in the largest amount of the magnetite solution to prevent aggregation of the OA-coated magnetite nanoparticles. However, it was our experience that the heptane interfered with stable generation of water droplets in a flow-focusing device made of PDMS and even dissolved an epoxy used for bonding between fittings and the PDMS

surface. Thus, the heptane was removed from 10 ml of the magnetite solution using a rotary evaporator (Rotavapor R-200). The evaporator was maintained at 70 °C for about 5 min until a slurry of nanoparticles was formed. The slurry was adjusted to the original particle concentration by adding 10 ml of pure oleic acid. The mixture was then dispersed in a bath ultrasonic cleaner (Branson 1510) for 5 min to produce MNOA with a concentration of $\sim 7.59 \text{ mg ml}^{-1}$. The solution was briefly agitated under ultrasound to ensure redispersion of the MNOA before use.

Fabrication of microfluidic routing device

Figure 3(a) shows a schematic of the PDMS microfluidic device comprising two parts: (1) a flow focusing geometry for droplet formation and (2) a main channel with three side channels to which droplets are directed. The widths of all channels of the flow-focusing region were 100 μm . The width of the main channel (W_0) was 400 μm , and the width of each side channel (W_1 , W_2 and W_3) was 133, 190, and 222 μm , respectively. The depth of all channels was 97 μm .

A PDMS sheet incorporating the microchannels was fabricated using a standard soft lithography technique.³¹ The PDMS substrate was punched for access holes and irreversibly sealed to a glass slide after an oxygen plasma treatment. Then, microfluidic fittings (LabSmith) were glued onto the inlet positions of the PDMS sheet. The PDMS microfluidic device was connected to syringe pumps (neMESYS, Cetoni GmbH) through capillaries (ID = 179 μm , OD = 354 μm , Polymicro Technologies) as shown in Fig. 3(b). The curved main channel was aligned with the disc magnet held by a microscope platform. DI water was injected into one inlet (denoted as “D”) while MNOA was introduced into the other inlet (denoted as “C”). The ratio of flow rates of water to MNOA was fixed at 0.02 throughout the droplet routing experiments.

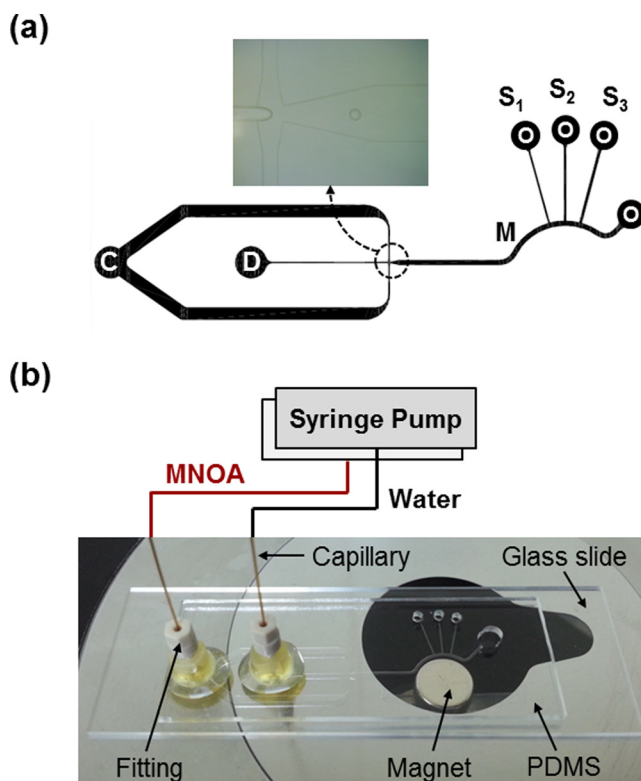


FIG. 3. Design and setup of the microfluidic droplet routing device. (a) AutoCAD drawing of the device consisting of two inlets (dispersed and carrier phases denoted by “D” and “C,” respectively), a flow-focusing junction and a main channel (M) with three side channels (S_1 , S_2 , and S_3). Outlets are denoted by “O.” (b) The microfluidic device setup on a microscope stage where a disc magnet is attached.

Instrumentation

To observe droplet behavior in the microchannels, images of droplet trajectories were obtained using an inverted fluorescence microscope (BX71W, Olympus) and a CCD camera (DP70, Olympus). Magnetic flux density was measured with a portable gauss meter (GM-1-ST, AlphaLAB). The magnetization curve of MNOA was obtained from a vibrating sample magnetometer (735 VSM, Lakeshore Cryotronics).

RESULTS AND DISCUSSION

Characteristics of water-in-MNOA droplets

To analyze the hydrodynamic properties of water-in-MNOA droplets, droplet size and behavior were compared when OA and MNOA were used as a carrier phase for droplet formation. As shown in Fig. 3(a), droplets were generated via the flow focusing technique. The carrier phase flow rates were 0.5, 1.0, and 1.5 ml h⁻¹, and the ratio of flow rates of the dispersed phase to the carrier phase was fixed at 0.02. For each flow rate, water-in-OA droplets with sizes of $107 \pm 0.5 \mu\text{m}$, $92 \pm 1.2 \mu\text{m}$, and $69 \pm 1.5 \mu\text{m}$ were obtained, while the sizes of water-in-MNOA droplets were $102 \pm 0.9 \mu\text{m}$, $88 \pm 1.4 \mu\text{m}$, and $63 \pm 2.0 \mu\text{m}$, respectively. The microfluidic device was operated at the Reynolds number of less than 1. Although the size distributions for each flow rate were quite narrow for both droplets, the water-in-MNOA droplets were slightly smaller than the water-in-OA droplets. This can be attributed to a higher viscosity of the MNOA as compared with that of the pure OA. In a stable condition, the MNOA has almost same viscosity as the pure OA due to its low volume fraction. Hence the higher viscosity could stem from the presence of aggregates. Our observations indicated that the trajectories of both droplets in the main channel were identical with no external fields applied (see below for details). We also observed that no magnetite particles penetrated into the water-in-MNOA droplets because the nanoparticles are coated with OA.

Centerline displacements at bifurcating junctions (without magnetic fields)

In a laminar flow through bifurcating junctions, displacements of the hydrodynamic centerline occur towards the side channels due to the flow diversion. In order to estimate such displacements, we performed 3-D numerical simulation on the laminar flow using COMSOL Multiphysics (COMSOL, Burlington, MA). In this case, the aspect ratio of the channel width to height was up to 4. This means that simple 2-D numerical simulation results would not represent true flow characteristics. Thus 3-D numerical simulations were carried out for a steady-state, laminar flow of a single phase fluid (oleic acid). Along with a no-slip condition at the walls, the boundary conditions of laminar inflow and zero pressure with no viscous stress were applied to the inlets and outlets, respectively. Simulations were run for three different flow rates of 0.51, 1.02, and 1.53 ml h⁻¹. Figure 4(a) shows the flow geometry and the simulation result for the flow rate of 1.02 ml h⁻¹ that displays velocity contours and streamlines through the middle of the channels. The black dotted arrow, a streamline that begins at the center of the main channel, indicates the displacements of the hydrodynamic centerline at each junction. Using the simulated streamlines, we calculated the centerline distances from the lower wall ($d_{c,1} = 200 \mu\text{m}$, $d_{c,2} = 227 \mu\text{m}$, $d_{c,3} = 269 \mu\text{m}$, and $d_{c,4} = 328 \mu\text{m}$) and the virtual boundary positions from the upper wall ($d_{s,1} = 75 \mu\text{m}$, $d_{s,2} = 98 \mu\text{m}$, and $d_{s,3} = 107 \mu\text{m}$) corresponding to each junction. These values remained almost unchanged for all the flow rates, and were used to predict the minimum offset distances (d_o) for each side channel. Accordingly, our routing device was designed based on the calculated results.

To visually assess the centerline displacements in experiments, the trajectory of moving droplets in the main channel was monitored. Flow rates of 0.02 ml h⁻¹ (water) and 1.0 ml h⁻¹ (OA) were used for the measurement. As shown in Fig. 4(b), droplets moved along the centerline of the main channel initially, and were laterally displaced toward the side channel as it passed through each junction. Once a droplet trajectory was established, no droplets moving out

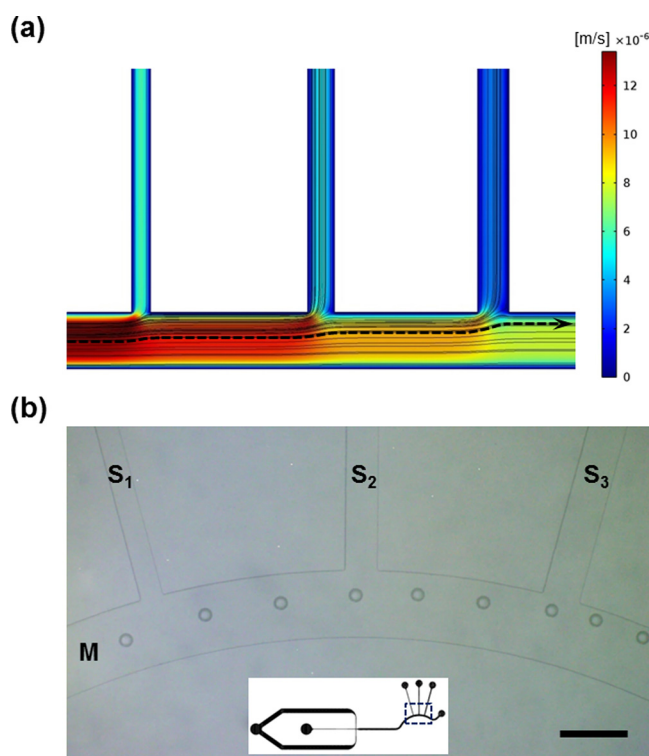


FIG. 4. (a) Velocity contours and streamlines obtained from the numerical simulations for a steady-state, laminar flow of OA with a flow rate of 1.02 ml h^{-1} . A straight main channel was adopted for simulation convenience. (b) An optical image of droplet trajectory in a main channel having three side channels. Flow rates for water (dispersed) and OA (carrier) phases were 0.02 ml h^{-1} and 1.0 ml h^{-1} , respectively. Scale bar, $400 \mu\text{m}$.

of the trajectory were observed. Assuming that the droplets were transported by the flow under no external forces, the droplet trajectory would represent the hydrodynamic centerline displacements. For verification of this hypothesis, we compared the numerical and experimental results with regard to the centerline displacements in Fig. 5(a). The simulation results were in good agreement with the experimental observations, indicating that the centerline displacement hypothesis was valid for the flow conditions. We also found that the analytical estimation of the virtual boundary positions ($d_{s,1} = 80 \mu\text{m}$, $d_{s,2} = 99 \mu\text{m}$ and $d_{s,3} = 105 \mu\text{m}$) is in good agreement with the simulation results as shown in Fig. 5(b).

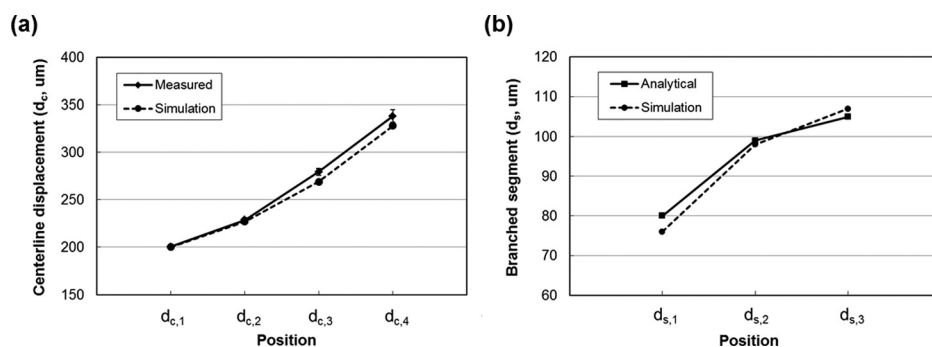


FIG. 5. (a) Comparison between the simulation and experimental results for centerline displacements (d_c) with respect to the positions along the main channel (refer to Fig. 2 for the positions of $d_{c,s}$). The experimental measurements were based on the trajectory of water-in-OA droplets without a magnetic field. (b) Comparison between the simulation results and analytical estimation for the virtual boundary positions (d_s).

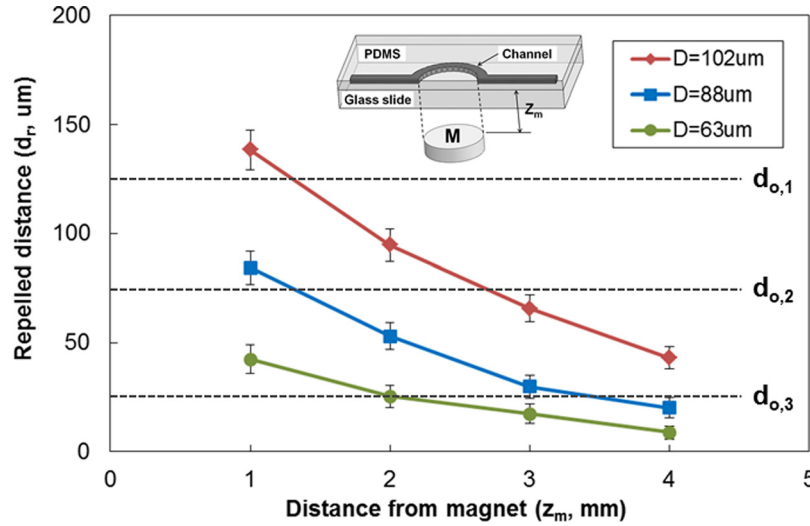


FIG. 6. Repelled distances (d_r) of droplets with respect to the magnet's top surface at four consecutive distances of $z_m = 1, 2, 3$, and 4 mm below the channel bottom. The repelled distances were measured at the middle of the curved segment for three different sizes of droplets ($63, 88$, and $102 \mu\text{m}$). The dotted lines represent the minimum offset distances required for a droplet to be directed to a side channel ($d_{o,1} = 125 \mu\text{m}$, $d_{o,2} = 75 \mu\text{m}$, and $d_{o,3} = 24 \mu\text{m}$).

Droplet repulsion with magnetic fields

To characterize the effect of the repelling force on droplets, the magnet's positions relative to the microchannel were related to the deflection of droplets from the hydrodynamic centerline. To this end, we used the microfluidic device, but had no side channels (see inset in Fig. 6). This was to separate the sole contribution of the repelling force from the hydrodynamic effects associated with the side channels. The water-in-MNOA droplets were generated under the same flow conditions described earlier.

Repelled distances of droplets (d_r) were measured with a disc magnet positioned at four consecutive distances of $1, 2, 3$, and 4 mm vertically below the channel. As shown in Fig. 6, the repelled distances grew rapidly as the magnet position became closer to the channel. The largest repelled distances were measured at its closest position (i.e., magnet in contact with a 1 -mm thick glass slide). The minimum offsets that would be required for droplets to be directed into each side channel were marked by dotted lines ($d_{o,1} = 125$, $d_{o,2} = 75$ and $d_{o,3} = 24 \mu\text{m}$). Note that the change in the repelled distances with the magnet's position had a similar pattern to that of the magnetic field gradient with its position (see Fig. S2 in the supplementary material³⁰). This indicated that the droplet repelling force is indeed proportional to the magnetic field gradient.

Routing of MNOA droplets

Given the relationship between droplet repulsion and magnet's position, we evaluated the performance of our droplet routing device. The routing of water-in-MNOA droplets into desired side channels was controlled by the distance of the magnet from the device. For a fixed droplet size, if the repelled distance was greater than the minimum offset allocated to a side channel, the droplets would flow into the side channel. In the case of routing droplets with an average size of $102 \mu\text{m}$, for example, about 92% of the droplets were routed into S_1 at $z_m = 1$ mm (Fig. 7(a)); about 99% of droplets into S_2 at $z_m = 2$ mm (Fig. 7(b)); about 76% of droplets into S_2 , while the rest of them were routed into S_3 at $z_m = 3$ mm (Fig. 7(c)); about 90% of the droplets were routed into S_3 with few droplets into the main outlet at $z_m = 4$ mm (Fig. 7(d)). These results are in good agreement with the repelled distance measurements shown in Fig. 6.

Table I lists the percentages of droplets that flowed into the side channels and the main channel at four different positions of the magnet. The experimental results exhibited good agreement with the proposed routing conditions (i.e., relation between the repelled distance and minimum offset,

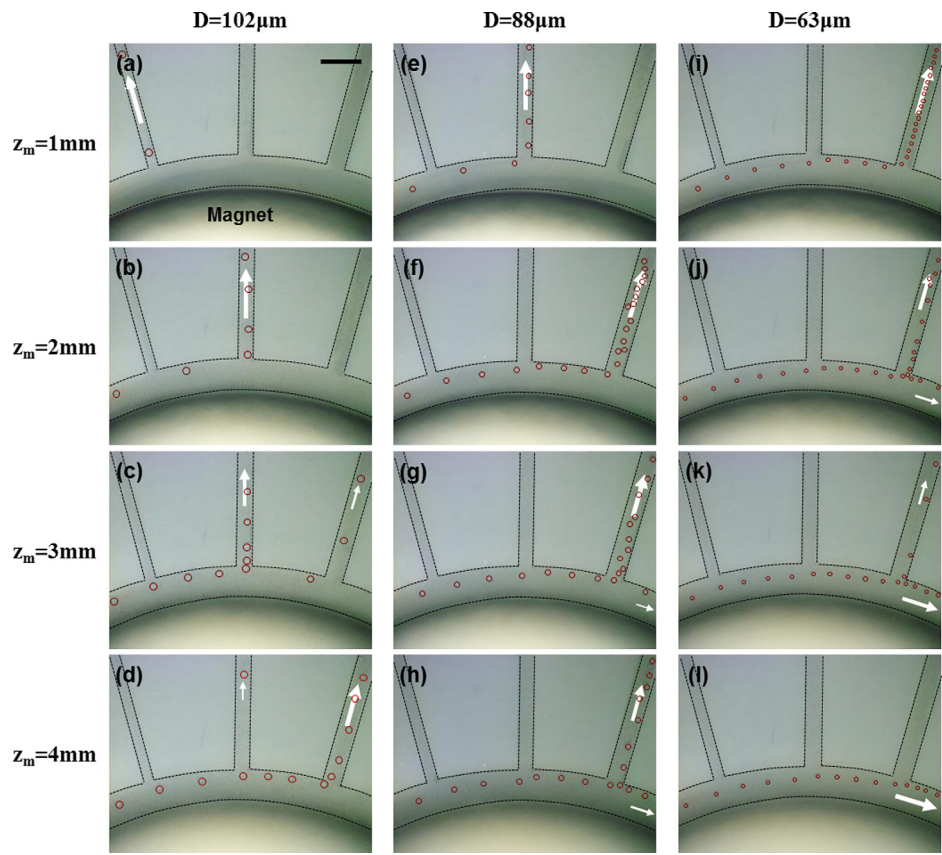


FIG. 7. Optical images of droplets that were routed into side channels by varying magnet positions. Three different sizes of droplets (63, 88 and 102 μm) were tested. The white arrows indicate the direction and portion of droplets being diverted into the side channel(s) and main channel. The dark black line at the bottom of each image is a shadow of the disk magnet. A $4\times$ objective was used. Scale bar, $500\mu\text{m}$.

TABLE I. Percentages of droplets of different sizes that were routed into each outlet with respect to the magnet's position. At least 400 droplets were counted for each case. Numbers in parentheses are the minimum offsets required for a droplet to be diverted to a corresponding side channel.

Mean droplet diameter (D , μm)	Distance from magnet (z_m , mm)	Average repelled distance (d_r , μm)	Percent (%) number of droplets flowing into each channel			
			S_1 (125 μm)	S_2 (74 μm)	S_3 (25 μm)	M
102.1	1.0	138.3	91.8	8.2	0	0
	2.0	94.7	0	98.6	1.4	0
	3.0	65.7	0	76.4	23.6	0
	4.0	43.0	0	8.1	90.1	1.8
87.5	1.0	84.3	0	100	0	0
	2.0	53.0	0	0	98.1	1.9
	3.0	29.7	0	0	73.8	26.2
	4.0	20.1	0	0	61.7	38.3
63.1	1.0	42.3	0	0	100	0
	2.0	25.3	0	0	64.6	35.4
	3.0	17.3	0	0	26.7	73.3
	4.0	8.7	0	0	0.9	99.1

$d_r > d_o$). However, a discrepancy was observed at S_3 (see Figs. 7(g) and 7(j)). Since the flow was slowest through S_3 (see Fig. 4(a)), the spacing between the droplets in S_3 was only $\sim 260 \mu\text{m}$, and some of the droplets bounced back off the preceding droplets. Thus, the bounced droplets were redirected to the main flow, resulting in a reduced routing efficiency. This problem may be alleviated if inclined side channels are used. Note that repulsion-based droplet routing in four outlet device would not be possible without being combined with the hydrodynamic flow pattern. Given a typical repulsion distance ranging up to $\sim 250 \mu\text{m}$,²⁰ a pure repulsion-based routing approach is likely to be limited to only a couple of outlet channels (with a channel width of $\sim 100 \mu\text{m}$). Meanwhile, our method exhibits increased flexibility in terms of routing capacity achievable with relatively smaller repelled distances and the number of outlets to be routed because of the simultaneous adaption of hydrodynamic centerline displacement effects.

The droplet repelling force is also proportional to the droplet volume according to Eq. (1), meaning that the repelled distances can be varied depending on the size of the droplets. Three different sizes of droplets were routed into different side channels with a magnet position fixed to 1 mm below the channel bottom (see Figs. 7(a), 7(e), and 7(i)). This suggests that our routing scheme could be used for continuous, size-dependent droplet discrimination at a fixed magnet position. Though the capability of routing larger size of droplets can be improved due to an increase in the repelled distance, there is a limitation on the droplet sizes for the improvement. For example, if droplets of a radius equal to or larger than the virtual boundary distance (d_s) corresponding to a side channel move along the upper wall, the droplets will undergo a deformation or break-up at the channel entrance, resulting in no successful droplet routing (i.e., in case of solid particles of the same size, they will not divert into but only pass by the channel entrance). Hence, the routing of large droplets can be improved when a radius of the droplets is less than the virtual boundary distance for the side channel.

Although large size of droplets (say, $> 100 \mu\text{m}$ in diameter) has been often used in cell screening assays,^{32,33} it would be more beneficial if droplet size is further reduced. In such a case, the routing capacity will be reduced, commensurate with a decrease in the repelled distance. In order to maximize the routing capacity for smaller size of droplets, the following parameters may be considered:

- (1) scale-down of channel dimensions (to reduce minimum offset distances, d_o),
- (2) use of higher field strength magnets (to have wider repelled distance ranges that facilitate discrimination of droplets in multiple outlets),
- (3) reducing distance between channels and magnet surface (to increase repelled distances, d_r).

CONCLUSIONS

We demonstrated droplet routing in a microchannel with four outlets (one main and three side outlets) using MNOA as the carrier phase. Water-in-MNOA droplets were manipulated using a combination of magnetic field and hydrodynamic laminar flow pattern, which required relatively small repulsion distances for droplet routing. Droplet trajectories were characterized in both the presence and absence of a disc magnet, and the numerical simulation results were in good agreement with the experimental measurements. Droplets with different diameters of 63, 88, and $102 \mu\text{m}$ were selectively routed into desired outlets simply by varying the magnet's positions. The routing method can be operated in dual modes: (1) an active mode for on-demand droplet routing by varying magnet positions; (2) a passive mode for continuous, size-based droplet separation at a fixed magnet position. We also anticipate that this routing module will not only allow selective enrichment of specific cells or biological entities, but also facilitate the integration of probes into fully automated lab-on-a-chip devices incorporating closed-loop feedback control.

ACKNOWLEDGMENTS

This research was supported by the Basic Science Research Program through the National Research Foundation of Korea (NRF) funded by the Ministry of Education, Science and Technology (2012R1A6A1029029 and 2013R1A2A2A01014234).

- ¹B. Zheng, L. S. Roach, and R. F. Ismagilov, *J. Am. Chem. Soc.* **125**, 11170–11171 (2003).
- ²M. M. Kiss, L. Ortoleva-Donnelly, N. R. Beer, J. Warner, C. G. Bailey, B. W. Colston, J. M. Rothberg, D. R. Link, and J. H. Leamon, *Anal. Chem.* **80**, 8975–8981 (2008).
- ³S. Köster, F. E. Angilè, H. Duan, J. J. Agresti, A. Wintner, C. Schmitz, A. C. Rowat, C. A. Merten, D. Pisignano, A. D. Griffiths, and D. A. Weitz, *Lab Chip* **8**, 1110–1115 (2008).
- ⁴J. Thiele, A. R. Abate, H. C. Shum, S. Bachtler, S. Förster, and D. A. Weitz, *Small* **6**(16), 1723–1727 (2010).
- ⁵Y. Hennequin, N. Pannacci, C. P. Torres, G. Tetradis-Meris, S. Chapuliot, E. Bouchaud, and P. Tabeling, *Langmuir* **25**(14), 7857–7861 (2009).
- ⁶L. Mazutis, J. Gilbert, W. L. Ung, D. A. Weitz, A. D. Griffiths, and J. A. Heyman, *Nat. Protoc.* **8**(5), 870–891 (2013).
- ⁷G. Du, J. Pan, S. Zhao, Y. Zhu, J. M. Toonder, and Q. Fang, *Anal. Chem.* **85**, 6740–6747 (2013).
- ⁸L. Mazutis, J. Baret, and A. D. Griffiths, *Lab Chip* **9**, 2665–2672 (2009).
- ⁹J. Clausell-Tormos, A. D. Griffiths, and C. A. Merten, *Lab Chip* **10**, 1302–1307 (2010).
- ¹⁰F. Sarrazin, L. Prat, N. Di Miceli, G. Cristobal, D. R. Link, and D. A. Weitz, *Chem. Eng. Sci.* **62**, 1042–1048 (2007).
- ¹¹J. R. Kovac and J. Voldman, *Anal. Chem.* **79**, 9321–9330 (2007).
- ¹²J. Baret, O. J. Miller, V. Taly, M. Ryckelynck, A. El-Harrak, L. Frenz, C. Rick, M. L. Samuels, J. B. Hutchison, J. J. Agresti, D. R. Link, D. A. Weitz, and A. D. Griffiths, *Lab Chip* **9**, 1850–1858 (2009).
- ¹³A. R. Abate, J. J. Agresti, and D. A. Weitz, *Appl. Phys. Lett.* **96**, 203509 (2010).
- ¹⁴T. Franke, A. R. Abate, D. A. Weitz, and A. Wixforth, *Lab Chip* **9**, 2625–2627 (2009).
- ¹⁵K. Ahn, C. Kerbage, T. P. Hunt, R. M. Westervelt, D. R. Link, and D. A. Weitz, *Appl. Phys. Lett.* **88**, 024104 (2006).
- ¹⁶M. R. Vincent, R. Wunenburger, and J. Delville, *Appl. Phys. Lett.* **92**, 154105 (2008).
- ¹⁷J. R. Dorvee, A. M. Derfus, S. N. Bhatia, and M. J. Sailor, *Nature Mater.* **3**, 896–899 (2004).
- ¹⁸N. Pamme and C. Wilhelm, *Lab Chip* **6**, 974–980 (2006).
- ¹⁹K. Zhang, Q. Liang, S. Ma, X. Mu, P. Hu, Y. Wang, and G. Luo, *Lab Chip* **9**, 2992–2999 (2009).
- ²⁰K. Zhang, Q. Liang, X. Ai, P. Hu, Y. Wang, and G. Luo, *Lab Chip* **11**, 1271–1275 (2011).
- ²¹A. Chen, T. Byvank, W.-J. Chang, A. Bharde, G. Vieira, B. L. Miller, J. J. Chalmers, R. Bashird, and R. Sooryakumar, *Lab Chip* **13**, 1172–1181 (2013).
- ²²O. Osman, S. Toru, F. Dumas-Bouchiat, N. M. Dempsey, N. Haddour, L.-F. Zanini, F. Buret, G. Reyne, and M. Frénéa-Robin, *Biomicrofluidics* **7**, 054115 (2013).
- ²³Y. Tan, J. S. Fisher, A. I. Lee, V. Cristini, and A. P. Lee, *Lab Chip* **4**, 292–298 (2004).
- ²⁴M. Yamada, M. Nakashima, and M. Seki, *Anal. Chem.* **76**, 5465–5471 (2004).
- ²⁵M. Yamada and M. Seki, *Lab Chip* **5**, 1233–1239 (2005).
- ²⁶Y. Tan, Y. L. Ho, and A. P. Lee, *Microfluid. Nanofluid.* **4**, 343–348 (2008).
- ²⁷M. Chabert and J. Viovy, *Proc. Natl. Acad. Sci.* **105**(9), 3191–3196 (2008).
- ²⁸A. Winkleman, K. L. Gudiksen, D. Ryan, and G. M. Whitesides, *Appl. Phys. Lett.* **85**, 2411 (2004).
- ²⁹H. Bruus, *Theoretical Microfluidics* (Oxford University Press, New York, 2007).
- ³⁰See supplementary material at <http://dx.doi.org/10.1063/1.4894748> for a magnetization curve for magnetite (Fe₃O₄) nanoparticles and a magnetic flux density variation with respect to the magnet position.
- ³¹G. Kim, S. Song, J. Lee, and J.-M. Kim, *Langmuir* **26**(23), 17840–17842 (2010).
- ³²E. Brouzes, M. Medkova, N. Savenelli, D. Marran, M. Twardowski, J. B. Hutchison, J. M. Rothberg, D. R. Link, N. Perrimon, and M. L. Samuels, *Proc. Natl. Acad. Sci.* **106**(34), 14195–14200 (2009).
- ³³J. Clausell-Tormos, D. Lieber, J.-C. Baret, A. El-Harrak, O. J. Miller, L. Frenz, J. Blouwolff, K. J. Humphry, S. Köster, H. Duan, C. Holtze, D. A. Weitz, A. D. Griffiths, and C. A. Merten, *Chem. Biol.* **15**, 427–437 (2008).